

# Fatigue crack growth rates in high pressure hydrogen gas for multiple X100 pipeline welds accounting for crack location and residual stress

Joseph A. Ronevich<sup>1</sup>, Eun Ju Song<sup>1</sup>, Zhili Feng<sup>2</sup>, Yanli Wang<sup>2</sup>, Christopher D'Elia<sup>3</sup>, Michael R. Hill<sup>3</sup>

<sup>1</sup> Sandia National Laboratories, Livermore, CA, USA

<sup>2</sup> Oak Ridge National Laboratory, Oak Ridge, TN, USA

<sup>3</sup> Department of Mechanical and Aerospace Engineering, University of California, Davis, Davis, CA, USA

Keywords: Hydrogen embrittlement, residual stress, welds, heat affected zone, fatigue crack growth rate

## Abstract:

Fatigue crack growth rates (FCGR) of multiple X100 pipeline steel welds and heat affected zones were measured in high-pressure hydrogen gas to investigate their behavior compared to lower strength pipeline welds. A total of five high strength welds and two heat affected zones (HAZ) were examined all of which were fabricated using the same X100 base material. Different welding wires and techniques were used to fabricate the welds to provide a variety of end products to evaluate susceptibility to fatigue in high pressure hydrogen gas. Residual stresses were measured for each weld and HAZ using the slitting method and the effect of residual stress on the stress intensity factor,  $K_{res}$ , was determined. Using  $K_{res}$ , the fatigue crack growth rate curves were corrected to remove the effects of residual stress by examining the influence of  $K_{res}$  on stress ratio,  $R$ . Comparisons were then made between the high strength welds, which were corrected for residual stress, and lower strength welds from the literature. It was found that the higher strength welds and heat affected zones exhibited comparable fatigue crack growth rates to lower strength welds, as the FCGR data of the high strength welds overlaid the lower strength welds. **This suggests that despite distinct differences in strength and microstructure between the different welds, hydrogen-assisted fatigue crack growth susceptibility is similar. A comparison was made between the  $K_{res}$  measured in extracted coupons and residual stress estimates provided in relevant welded pipe assessment standards such as API 579-1/ASME FFS-1. It was found the residual stress values in the test coupons extracted from welded pipe were significantly lower than those expected in the intact welded pipes and highlights the importance in quantifying and removing residual stresses when fatigue assessments are being made.**

## 1. Introduction:

Over 1,500 km of steel pipelines have been used to transport gaseous hydrogen throughout the U.S. safely and reliably over the years [1]. Hydrogen pipelines were constructed out of low strength steels and have been used to service refineries with relatively constant demand. The pipelines operate with minimal pressure fluctuations and modest pressures ( $<7$  MPa). As a result, the safety history of these pipes has been relatively good over the years [1]. As an economy develops for alternative fuels, a greater demand is expected for hydrogen to help replace non-renewable energy resources, and steel pipelines can transmit gaseous hydrogen over long distances much cheaper than alternative methods such as by tanker trucks [2]. One means to improve cost effectiveness of gaseous transmission of hydrogen is through operation at higher pressures to increase throughput. Lower strength steels which have conventionally been used in hydrogen pipelines may be limited in their operating pressures which prevents cost savings that could be realized by operating at higher pressures. Higher strength pipes offer a larger operating envelope for higher pressures and large diameter pipes to be used. As hydrogen demand fluctuates, there is potential for fatigue loading

45 on pipelines which brings about a different failure mode that has not been examined on high strength steel  
46 pipeline welds. Recent work [3-9] has examined the behavior of a variety of strength grades of pipelines  
47 subjected to cyclic loading in hydrogen gas. The results showed similar accelerated fatigue crack growth  
48 for all the pipeline grades regardless of strength, which is counter to the conventional assumption that higher  
49 strength steels are more susceptible to hydrogen embrittlement. One area that has negligible research but  
50 needs to be investigated before higher strength pipes can be considered for deployment, is the behavior of  
51 welds in a cyclic hydrogen environment. Welds are a critical part of pipelines and often failures are  
52 associated with welds [10] yet the weld behavior under fatigue in the presence of hydrogen has not been  
53 explored, particularly in higher strength welds. **The microstructure of welds is likely different than the base  
54 metals, although a comparison of FCGR for a variety of pipelines tested in high pressure hydrogen have  
55 shown negligible effects of microstructure [11].** Welds are more likely to have defects or stress  
56 concentrators due to misalignment or underfilling of the weld joint which could lead to initiation and  
57 extension of cracks. In addition, residual stresses are innate in welds which means that residual stress would  
58 be additive to the applied stress due to the gas pressure. Furthermore, higher strength welds are likely to  
59 retain higher residual stresses meaning the effects of residual stress could be more significant on the  
60 absolute stress experienced by the pipe. Only a few studies [4, 12, 13] have examined fatigue behavior of  
61 welds **in hydrogen**, which were from lower strength pipes, and residual stresses were not measured in these  
62 studies to examine their influence. One study [3] did examine a high strength weld and remove residual  
63 stress effects, but this was examined on a single weld and the results might not be applicable to other  
64 welding techniques and conditions. All of these factors motivate the current research to investigate the  
65 fatigue behavior of multiple high strength pipeline steel welds in high pressure hydrogen gas and examine  
66 the influence of residual stress on their behavior. **The intention of this paper is to examine the behavior of  
67 a broad range of welds to assess their behavior rather than to try and optimize the welding process for  
68 hydrogen resistance.**

69

## 70 **2. Methods**

### 71 *2.1 Weld fabrication*

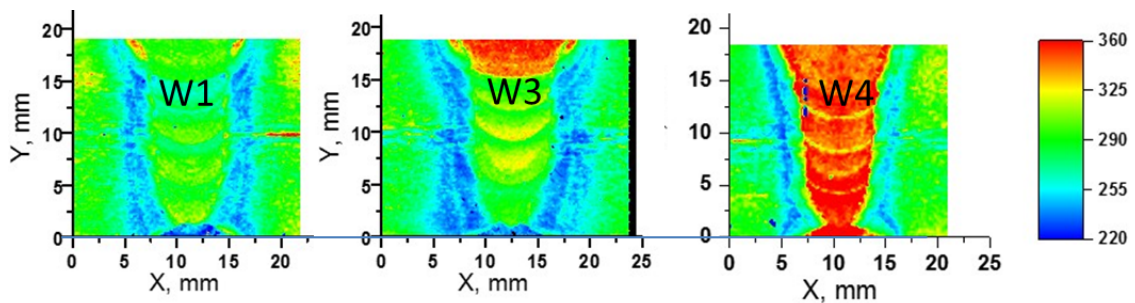
72 An experimental X100 girth welded pipe studied previously [3] was used as the test material for  
73 this study. The pipe is 19 mm thick with a diameter of 1.3 m with a measured yield strength of 731 MPa  
74 and ultimate tensile strength of 868 MPa in the longitudinal direction. The composition of the X100 pipe is  
75 listed in Table 1. As the X100 pipe was an experimental pipe (labeled as X100A), the details of the welding  
76 process were not provided including the filler wire used. **From this original X100A welded pipe, sections  
77 of the base metal were removed in longitudinal strips such that subsequent welds were performed in the  
78 longitudinal direction, effectively making seam welds.** From these X100A pipe sections, four welds were  
79 fabricated at Oak Ridge National Laboratory (ORNL) using different welding filler metals and different  
80 welding techniques. Tables 2a and 2b show a detailed list of the welding parameters. Three different filler  
81 metals were used for welds W1, W3, and W4 and a fourth weld was fabricated via friction stir welding  
82 (FSW). W1 used matching strength filler metal ER100S-G from Lincoln Elec. W3 used over-matching  
83 filler metal ER120S-G from ESAB. The W4 weld used a novel welding consumable developed by ORNL  
84 in collaboration with the U.S. Army [14]. This weld consumable was specifically designed and formulated  
85 to prevent hydrogen embrittlement in welds of high-strength armored steels, based on the principle of low  
86 temperature phase transformation (LTPT) to reduce or eliminate the high tensile residual stresses in the  
87 weld region. In W4, a residual stress distribution was developed to promote compressive residual stress  
88 near the weld root. One of the advantages of using this weld wire is that it no longer requires the pre-heat  
89 during fabrication of the welds, thus simplifies the welding process and reduces fabrication cost. For the

90 FSW, pipe sections were welded longitudinally in a double-sided, double-pass, full penetration  
91 configuration. A Polycrystalline Cubic Boron Nitride (PCBN) tool was used in FSW. The tool had a  
92 threaded, tapered probe with three flats, 12 mm in length. It had a convex, scrolled shoulder approximately  
93 35 mm (1.4 inch) in diameter that engaged with the workpiece, resulting in a weld crown width of  
94 approximately 25 mm (1 inch). The first pass of each stir weld was applied to the inner diameter (ID) of  
95 the pipe. The second pass was made from the outer surface side (OD) in the same welding direction as the  
96 first weld pass, overlapping the advancing side (AS) of pass 2 with the retreating side (RS) of pass 1 and  
97 the retreating side of pass 2 with the advancing side of pass 1.

98 Tensile testing was performed in air on samples perpendicular to the welding direction with the  
99 gage section encompassing both the weld and heat affected zones. Table 3 shows the resulting yield and  
100 tensile strengths of the **five welds examined in this study**. Failure often occurred in the HAZ as opposed to  
101 the weld metal, therefore only the YS and UTS values were reported. The nominal strain rate was  $10^{-3}/s$ .  
102 **Hardness maps of the welds are shown Fig. 1 for the X100 W1, W3, W4, and FSW showing the Vickers**  
103 **Hardness (VH) values. A hardness map was not collected of the X100A weld. All of the maps show a**  
104 **common trend; hardness values in the weld are equal to or greater than the base metal and reduced hardness**  
105 **in the HAZ, the HAZ softening effect commonly associated with welding of high strength steels. Two**  
106 **locations identified as (1) and (2) are shown in Figure 1 for the FSW. These locations correspond to the**  
107 **micrographs of the FSW (Figure 2g) and FSW-HAZ (Figure 2h) and are discussed below.**

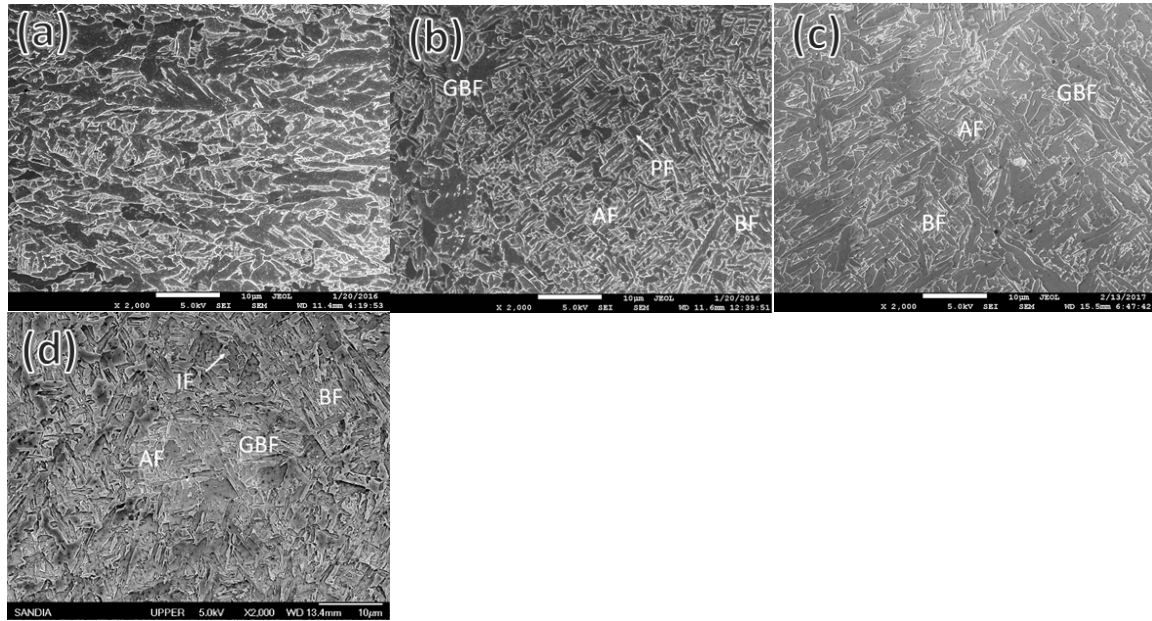
108 Figure 2 shows optical images of the microstructures of the different welds as compared to the  
109 original X100A base metal. The microstructure of the X100A base metal consists of a mixture of fine ferrite  
110 and bainite. Similar constituents are observed in the W1, W3, and FSW but with varying densities. The  
111 X100 W4 represents the most unique microstructure, predominately martensite which is characteristic of  
112 the LTPT weld wire. Tempered martensite was also present in the interpass region, caused by the tempering  
113 effect of subsequent weld pass to the previous weld pass. It is important to note that the martensite of the  
114 LTPT weld wire in W4 weld is much more stable than the microstructure constituents in commercial weld  
115 wires in W1 and W3. It is particularly evident in the W3 weld, where the tempering effect from the  
116 subsequent weld passes substantially reduced the hardness (strength) of a weld pass from  $\sim 360Hv$  to the  
117 range of 250-300Hv. The microstructures of the high strength welds are much finer than observed in other  
118 lower strength welds in the literature [4, 12].

119



120

121 Figure 1 – Vickers hardness maps for the X100 W1, W3, W4 and FSW. No hardness data were collected  
122 of the X100A weld.



123

124

125 Figure 2 – Scanning electron microscope images of X100 base metal,  
 126 (b) X100A weld, (c) X100 W1, (d) X100 W3, (e) X100 W4, (f) X100 FSW. Different morphologies of  
 127 ferrite and bainite are defined: GBF-grain boundary ferrite, AF-acicular ferrite, BF-bainitic ferrite, IF-  
 128 idiomorphous ferrite.

129

**Table 1: Chemical Composition of X100 Base Metal (wt .pct)**

Fe	C	Mn	P	S	B	Si	Cu	Ni	Cr	Mo	Nb	Ti	Al
Bal	0.085	1.69	0.013	<0.001	0.0015	0.26	0.14	0.24	0.19	0.17	0.047	0.017	0.029

130

131

**Table 2a: Weld parameters of X100 W1, W3, W4**

	W1	W3	W4
<b>Root pass</b>	ER70S-6 (pass 1)	ER70S-6 (pass 1)	LTTW HV 1764
<b>Weld pass (2-6)</b>	ER100S-G (Lincoln Elec.)	ER120S-G (ESAB)	LTTW HV 1764
<b>preheat</b>	100C	125C	N/A
<b>Inter pass Temp</b>		125C	<55C
<b>Shielding gas</b>	Ar/Co2 (95/5), 1.13 CMH (40 CFH)	Ar/Co2 (95/5), 1.13 CMH (40 CFH)	Ar/Co2 (95/5), 1.13 CMH (40 CFH)
<b>Heat input</b>	Pass 1=370 kJ/m (9.4 kJ/in)	Pass 1= 413 kJ/m (10.5 kJ/in)	Pass 1=472 kJ/m (12 kJ/in)
	Pass 2-6 = 626-732 kJ/m (15.9-18.6 kJ/in)	Pass 2-6= 665-866 kJ/m (16.9-22 kJ/in)	Pass 2-5= 732-835 kJ/m (18.6-21.2 kJ/in)
<b>Travel speed</b>	Pass 1= 457 mm/min (18 in/min)	Pass 1= 457 mm/min (18 in/min)	Pass 1= 610 mm/min (24 in/min)
	Pass 2-6= 30.5 cm/min (12 in/min)	Pass 2-6= 25.4-30.5 cm/min (10-12 in/min)	Pass 2-6= 40.6 cm/min (16 in/min)

132

133

**Table 2b: Weld parameters of X100 FSW**

Parameter	Pass 1 & 2
-----------	------------

<b>Welding speed</b>	50.8 mm/min
<b>Tool Rotation Rates (welding)</b>	125 rpm
<b>Tool Rotation Rate (plunge)</b>	270 rpm
<b>Tool Tilt Angle</b>	0 degrees
<b>Axial Control Force Range*</b>	75.62 kN

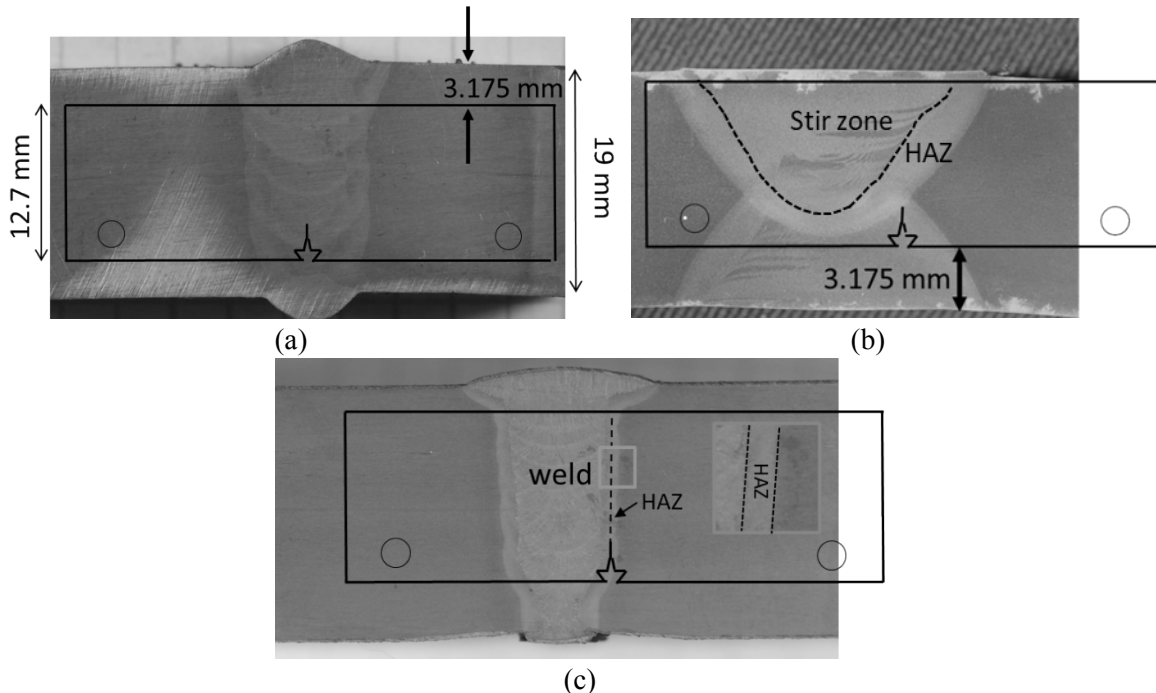
\*Manually adjusted throughout each weld pass within this range

**Table 3:** Yield strength and ultimate tensile strength of fabricated welds

	<b>X100A weld</b>	<b>X100 W1</b>	<b>X100 W3</b>	<b>X100 W4</b>	<b>X100 FSW</b>
<b>Yield strength (0.2% offset)</b>	705	580	720	740	605
<b>Ultimate tensile strength</b>	791	851	841	889	780

## 2.2 Coupon Preparation

Test coupons were removed from the X100A welded pipe to allow for subsequent fatigue crack growth rate tests or residual stress measurements. Eccentrically loaded single edge tension (ESE(T)) coupons, described in ASTM E647-11 [15], were removed from the X100A weld such that crack growth was in the radial direction. For all ESE(T) coupons, the loading direction was applied perpendicular to the welding direction. It should be noted that the loading direction for the X100A weld was in the original pipe's longitudinal direction; however, because the subsequent welds W1, W3, W4, and FSW were effectively seam welds (as mentioned in Section 2.1), the loading direction in these ESE(T) coupons was in the circumferential direction with respect to the original pipe. ESE(T) coupons were machined with no side-grooves, a width ( $W$ ) = 12.7 mm, thickness ( $B$ ) = 3.18 mm, and precrack starter notch length-to-width ratio ( $a_n/W$ ) = 0.2. Figure 3a shows a schematic overlay of ESE(T) extraction location for a crack in the weld metal. Weld metal (weld) coupons had the notch positioned in the center of the weld with coupons for all welds tested: X100A, W1, W3, W4, and FSW. In addition, coupons were extracted with a crack in the heat affected zone (HAZ) for two welds, with coupons designated as X100 FSW HAZ (Fig. 3b) and X100A HAZ (Fig. 3c). The notch of HAZ specimens were positioned outside of the weld metal (Fig. 3c) or stir zone (Fig. 3b) but still in the heat affected zones. The light grey regions (e.g. halo) shown in Figures 1b and 1c are the etching response of the heat affected zones which is where the notches were positioned. A higher magnification image of the position of the notch is shown in Fig. 1c. The ESE(T) coupons were either used for FCGR measurements or residual stress measurements. Since both are effectively destructive tests, a minimum of two measurements of FCGR and residual stress were made on each weld to ensure consistency and allow for comparisons. In addition to the ESE(T) coupons with the machined notches, coupon blanks were removed from the FSW without the notch to facilitate easier measurement of residual stresses. In addition to the ESE(T) coupons, compact tension (C(T)) coupons were extracted from the X100 base metal and used for subsequent FCGR and residual stress measurements as reported in [3].



162  
163

164  
165

166 Figure 3 – Schematic of ESE(T) coupon extraction locations from weld and HAZ. (a) X100 weld W1, (b)  
 167 X100 FSW HAZ, (c) X100A HAZ. Notch was positioned in approximate center of weld or HAZ such that  
 168 crack extended from inner to outer diameter.

169 *2.3 Fatigue Crack Growth Measurements*

170 Fatigue crack growth rate measurements were made on ESE(T) coupons in 21 MPa of high purity  
 171 (99.9999%) hydrogen gas at room temperature, 293 K. Fatigue loading was accomplished using a servo-  
 172 hydraulic load frame with a custom-built pressure vessel capable of delivering up to 22 kN of load  
 173 dynamically to the sample. The system is built using dynamic spring energized Teflon® U-cup seals which  
 174 allow for sealing between a pull-rod attached to the actuator and the pressure vessel. An internal load cell  
 175 is located in the pressure vessel to ensure proper measurement of load on the coupon. Displacement was  
 176 measured using a clip gauge. More details of the dynamic loading high-pressure system can be found in a  
 177 previous publication [16]. Before beginning the test, air in the pressure vessel was removed via a process  
 178 of evacuation and purging with high pressure helium. **Four successive purges were performed with inert  
 179 gas followed by vacuum for a minimum of 20 minutes, followed by four purges with hydrogen at 14 MPa,  
 180 before filling the vessel to the test pressure of 21 MPa hydrogen. Oxygen contents were measured of the  
 181 test gas following the completion of select tests and found to be consistently below 1 vppm.** Duplicate and,  
 182 in some cases, triplicate tests were performed on each weld at an applied load ratio of  $R_{app} = 0.5$  and  
 183 frequency of 1 Hz. The test pressure of 21 MPa was selected based on input from the ASME B31.12  
 184 Hydrogen Piping and Pipeline Code [17] committee and identified as an upper-bound for piping in the  
 185 future. Test frequencies have been shown to only modestly affect FCGR [18]; e.g. FCGRs were observed  
 186 to increase by a factor of 2 when test frequency was decreased from 1 Hz to 0.1 Hz and negligible changes  
 187 were observed below that frequency **for tests performed at constant  $\Delta K$  of  $17.5 \text{ MPa m}^{1/2}$ .** Fatigue crack  
 188 growth rate tests were run according to ASTM E647-11 [15] as either constant load amplitude or **positive**  
 189 **K-control** conditions. Results were consistent using either method. Crack length was determined using  
 190 unloading compliance and a seven-point polynomial was used to develop  $da/dN$  vs.  $\Delta K$  curves [15].  
 191 Following completion of the test, initial and final crack lengths were measured optically and used as fixed  
 192 bounds to correct the crack lengths measured by unloading compliance.

193 *2.4 Residual Stress Measurements*

194 Residual stress along the crack plane of ESE(T) coupons was measured using the slitting method  
 195 [19-21]. Each coupon was fixed with a metallic foil strain gauge bonded to the coupon back face in line  
 196 with the crack plane. A wire electric discharge machining (wire EDM) was used to extend a slit in  
 197 increments of depth along the crack plane, from the notch or front face toward the back face. Residual stress  
 198 as a function of distance from the front face,  $\sigma_{res}(x)$  was determined from strain versus slit depth data,  $\varepsilon(a)$ ,  
 199 using typical procedures [20, 21]. The residual stress intensity factor as a function of crack length,  $K_{res}(a)$   
 200 was also determined from strain versus slit depth data using the method described by Schindler [22]

$$201 \quad K_{res}(a) = \frac{E' d\varepsilon(a)}{Z(a) da} \quad (1)$$

202 where E' is the generalized planar elastic modulus, Z(a) is a geometry dependent influence function, and a  
 203 is crack length. Plane stress was assumed and therefore the generalized elastic modulus was assumed to be  
 204  $E' = E = 207$  GPa. The influence function Z(a) was available as an algebraic expression found in Schindler  
 205 and Bertschinger [23]. The derivative  $d\varepsilon(a)/da$  was determined by fitting a quadratic polynomial to a  
 206 moving array of 5 strain data points and evaluating the polynomial derivative analytically [3].

207 *2.5 Correction of Fatigue Crack Growth Rate Data Using Residual Stress Measurements*

208 The following methodology for removing residual stress effects from FCGR curves was outlined  
 209 previously in detail in [3] and is briefly described below. All FCGR tests were conducted at an applied load  
 210 ratio,  $R_{app} = 0.5$  which is defined as the minimum load,  $P_{min}$ , divided by the maximum load,  $P_{max}$  as shown  
 211 in equation 2

$$212 \quad R_{app} = K_{min-app}/K_{max-app} = P_{min}/P_{max} \quad (2)$$

213 Residual stress ( $K_{res}$ ) alters the total stress ratio,  $R_{tot}$ , by

$$214 \quad R_{tot}(a) = (K_{min-app}(a) + K_{res}(a))/(K_{max-app}(a) + K_{res}(a)) \quad (3)$$

215 where  $K_{min-app}(a)$  and  $K_{max-app}(a)$  are the cyclic stress intensity factors at a minimum and maximum applied  
 216 load. It is important to note that  $R_{tot}(a)$  is dependent on the magnitude of  $K_{res}(a)$ ; however,  $\Delta K$  is independent  
 217 of  $K_{res}(a)$  as it appears in both the maximum and minimum stress intensity factors, effectively canceling  
 218 (e.g.  $\Delta K = \Delta K_{app}$ ). So any influence of  $K_{res}(a)$  manifests itself as a change in total stress ratio ( $R_{tot}$ ) not  $\Delta K$ .

219 An analysis methodology was developed by Donald and Lados [24] and detailed by James [25] to  
 220 collapse data of different stress ratios to a single curve which can be useful for design. The first step was to  
 221 develop a normalized stress intensity factor ( $K_{norm}$ ) that was independent of load ratio as shown below

$$222 \quad K_{norm}(a) = (\Delta K(a))^{1-n} * (K_{max-app}(a) + K_{res}(a))^n \quad (4)$$

223 where n is a parameter for  $K_{max}$  sensitivity (n=1 makes  $K_{norm}$  depend only on  $K_{max}$  and n=0 makes  $K_{norm}$   
 224 depend only on  $\Delta K$ ). A value of  $n = 0.25$  was determined by plotting three FCGR curves for X100 base  
 225 metal tested in air at  $R = 0.1, 0.5,$  and  $0.7$  and adjusting  $n$  to best visual fit when the plot of the three curves  
 226 of  $da/dN$  vs  $K_{norm}$  collapsed [3]. The X100 base material was determined to be effectively residual stress  
 227 free and did not exhibit crack closure [3]. As testing in this current study was only performed at  $R_{app} = 0.5$ ,  
 228 determination of  $n$  was not possible for each weld; however, the value of  $n = 0.25$  is consistent with other  
 229 structural metals reported in the literature [24, 25] and therefore was employed for all corrections in this

230 current work on welds. Specific stress ratios  $\bar{R}$  were then employed by using the  $K_{norm}$  curve and the Walker  
231 equation [25] as shown below

$$232 \quad \Delta K_{corr} = K_{norm} * (1 - \bar{R})^n \quad (5)$$

233 where  $n = 0.25$ ,  $\bar{R}$  is 0.5, and the subscript corr indicates the data was corrected to account for the effect of  
234 varying  $R_{tot}(a)$ . In short, the data were corrected to force a stress ratio  $\bar{R}$  equal to 0.5 even though the  $R_{tot}(a)$   
235 varied due to non-zero  $K_{res}(a)$  in the welds.

### 236 3. Results and Discussion

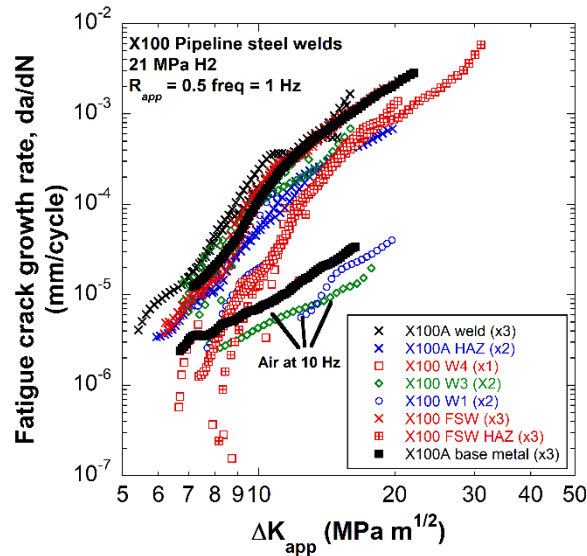
#### 237 3.1. Hydrogen accelerated fatigue crack growth measurements

238 The effect that hydrogen has on accelerating fatigue crack growth rates is easily observable in Fig.  
239 4 which shows  $da/dN$  vs  $\Delta K_{app}$  curves for high strength welds and heat affected zones tested in high pressure  
240 hydrogen gas. For comparison, fatigue crack growth rates were measured in air for X100 base metal and  
241 X100 W1 and W3 which exhibited significantly lower FCGR compared to in hydrogen, particularly in the  
242 higher  $\Delta K$  range. Above  $\Delta K = 10 \text{ MPa m}^{1/2}$ , the effect of hydrogen on FCGR is apparent and FCGRs were  
243 measured to be more than an order of magnitude faster in hydrogen than in air. Five different X100 welds  
244 were examined in high pressure hydrogen gas and the heat affected zones (HAZ) were examined in two of  
245 the welds (X100A and X100 FSW). Duplicate (x2) or triplicate (x3) tests were performed on most welds  
246 and the results are plotted in Fig. 4. The exception is X100 W4 in which only 1 test was successful, which  
247 was attributed to large compressive residual stresses which made extending a precrack challenging. It  
248 should be noted that successful extension of a precrack of X100 W4 was only possible by compression  
249 precracking under load control from -0.89 kN to -5.340 kN to extend the precrack for approximately 30,000  
250 cycles, followed by tension precracking to  $\sim a/W = 0.2$ .

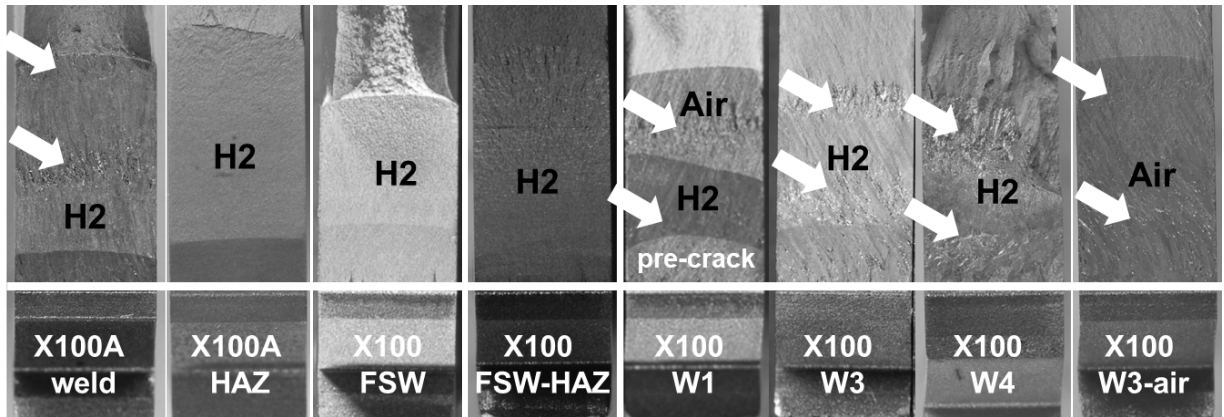
251 In general, the results were repeatable for each weld tested. Observing the data as a whole, the  
252 characteristic trends are similar in that accelerated rates start between  $\Delta K_{app}$  of 5 to 9  $\text{MPa m}^{1/2}$  and  
253 accelerate to over 30 times greater FCGR than in air at higher  $\Delta K_{app}$  values. The band of FCGRs however  
254 appears to be quite broad when compared to FCGR trends observed for pipeline base metals tested in  
255 previous work [3-9] in which the curves nearly overlay regardless of the pipe grade. However, replicate  
256 tests exhibited self-consistency, which suggests real trends among the different welds examined which are  
257 discussed. First, in general, the HAZ exhibited lower FCGR than their respective welds for the X100A and  
258 X100 FSW. Second, the original X100A weld appears to exhibit the highest fatigue crack growth rate of  
259 all the welds tested. However, before any significant conclusions can be made about these welds, it is  
260 important to note that although all the experiments were performed at applied load ratio of  $R_{app} = 0.5$ , the  
261 total stress ratio  $R_{tot}(a)$  was actually quite different for each weld due to the influence of residual stress. It  
262 will be shown in the next section the influence that  $K_{res}(a)$  has on  $R_{tot}(a)$  and the shift that can occur in these  
263 FCGR curves when residual stress effects are removed.

264 Following the fatigue testing in high pressure hydrogen gas, the samples were fatigued in air to  
265 failure to allow observation of the fracture surfaces for further examination and measurement of crack  
266 extension. A representative set of fracture surface images is shown in Fig. 5 for the five welds tested, along  
267 with two HAZ and one weld tested in air. The distinct regions are identified in X100 W1 are the initial  
268 precrack, fatigue in  $H_2$ , and post fatigue in air. The gas metal arc welds exhibit distinct features on the  
269 fracture surfaces that have been attributed to the individual welding passes, as described in previous work  
270 [3]. These features are identified by the white arrows in Fig. 5 for the X100A weld and X100 W1, W3, and

271 W4. The X100A HAZ, X100 FSW and X100 FSW-HAZ do not exhibit these features, as metal was not  
 272 added in layers in these regions as it was in the gas metal arc welds.



273  
 274 Figure 4 – Fatigue crack growth rate ( $da/dN$  vs  $\Delta K_{app}$ ) curves for X100 pipeline welds tested in 21 MPa  $H_2$   
 275 gas at applied  $R=0.5$  and frequency of 1 Hz. Tests were conducted in air at 10 Hz for comparison.

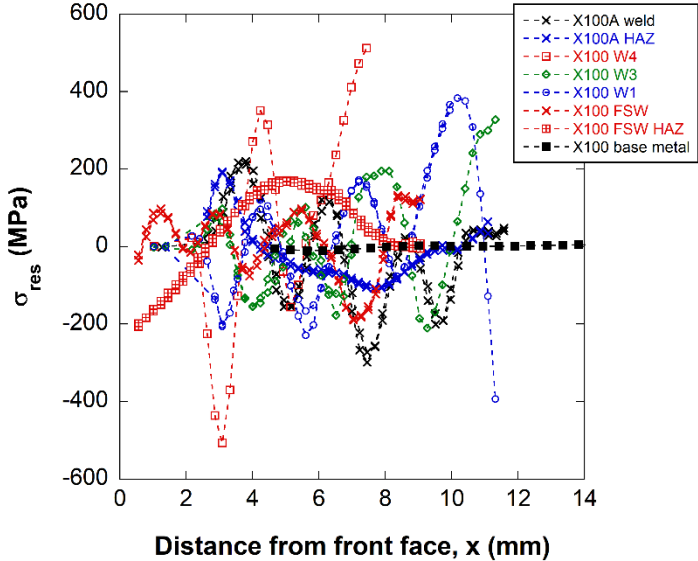


276  
 277 Figure 5 – Fracture surfaces of X100 welds tested in 21 MPa  $H_2$  gas and in air. Three distinct regions are  
 278 visible on most fracture surfaces as the crack extends from bottom to top as labeled in X100 W1: pre-crack  
 279 in air, fatigue in  $H_2$ , and post fatigue in air. Multi-pass arc welds (e.g. X100A weld, W1, W3, W4) are  
 280 distinguishable by periodic rough features associated with individual weld passes (white arrows).

281  
 282 *3.2. Residual stress measurements of welds*

283 Using the slitting method, residual stress as a function of distance from the front face was measured  
 284 for the 5 weld, 2 HAZ, and X100 base metal coupons, with data shown in Fig. 6. Duplicate tests were  
 285 performed and showed excellent repeatability which are plotted in Fig. 6 except for on X100 W4 in  
 286 which only a single test was performed. The duplicate tests overlay each other demonstrating the consistent  
 287 residual stresses in the test coupons. In most weld coupons, the measurements started from the existing  
 288 machined notch, beginning around 2.5 mm from the front and extended to approximately 12 mm. The X100

289 FSW and X100 FSW HAZ samples were prepared without a notch so those measurements began  
 290 approximately 0.5 mm from the front face. In all weld and HAZ coupons,  $x = 0$  mm was closest to the inner  
 291 diameter of the pipe with  $x$  increasing radially outward, as shown in Fig. 3. A C(T) coupon was used for  
 292 measurements on the X100 base metal which has a larger notch, and therefore, measurements were not  
 293 obtained until approximately 5 mm from the load line [3]. **It should be noted that the C(T) coupon**  
 294 **measurements were taken in the circumferential direction not the radial direction as it was for the welds**  
 295 **and HAZ.** All of the weld and HAZ coupons exhibited significant residual stress levels which varied  
 296 predominantly between +/- 200 MPa with some deviations outside of this range. Most notable is the X100  
 297 W4 which contained a highly compressive stress over -500 MPa around 3 mm. Repeated fluctuations in the  
 298 residual stress with distance were attributed to the periodic weld passes and are more prevalent in the gas  
 299 metal arc weld samples than the FSW or HAZ samples.

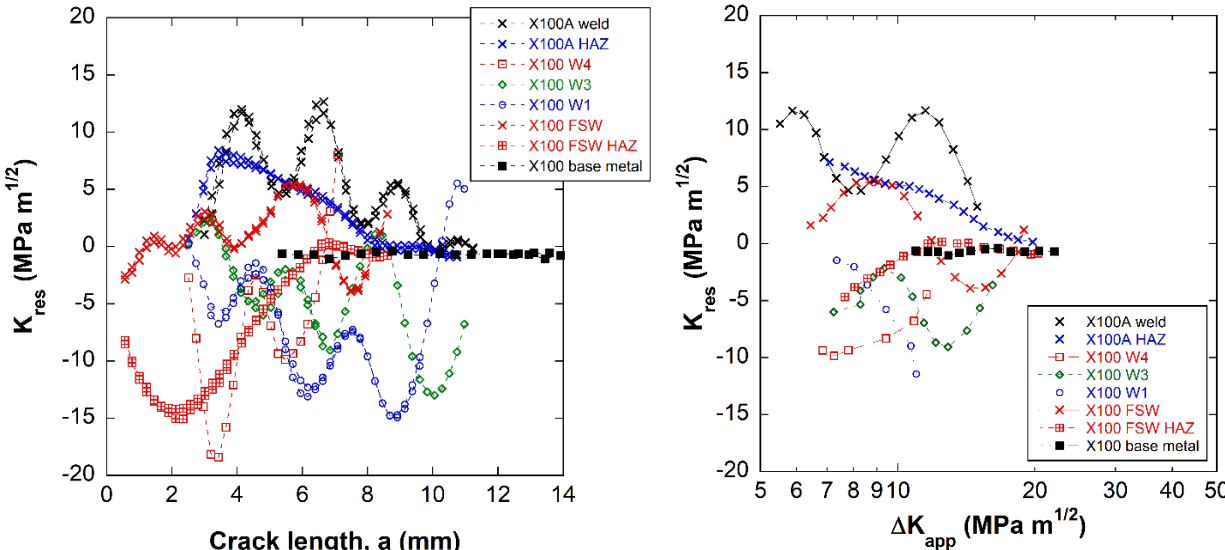


300  
 301 Figure 6 – Residual stress ( $\sigma_{res}$ ) as a function of distance from front face for X100 welds and base metal.  
 302 For each weld, two separate samples were measured, and the results are plotted, except for X100 W4 which  
 303 is only a single test. Negligible residual stress was measured in X100 base metal.

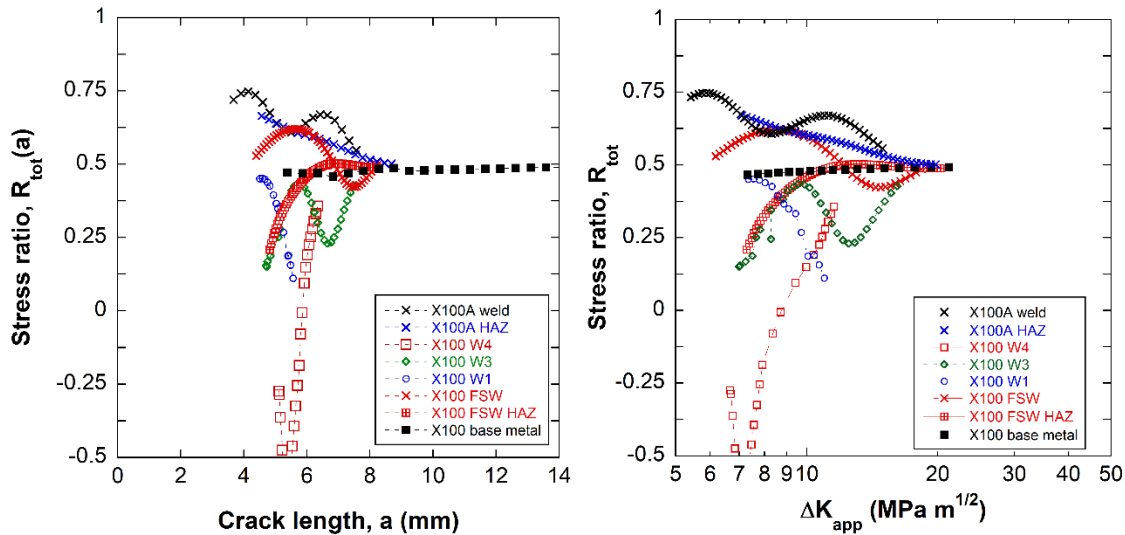
304 The residual stress intensity factor,  $K_{res}$ , as a function of crack length data from all coupons are  
 305 shown in Fig. 7a. Duplicate tests have good repeatability and there are significant differences in  $K_{res}$  for the  
 306 different weld and HAZ coupons. In Fig. 7a, the periodicity in  $K_{res}$  is more prevalent for the multi-pass  
 307 weld coupons compared to the smooth trends for the FSW and HAZ coupons. The X100 FSW HAZ coupons  
 308 exhibited a negative  $K_{res}$  at short crack lengths decaying to negligible values at longer crack lengths. The  
 309 X100 W4 coupon exhibited large negative  $K_{res}$  values at short crack lengths which diminished at longer  
 310 crack lengths. The X100A weld and HAZ coupons exhibited positive  $K_{res}$  at short crack lengths that  
 311 diminished to negligible values at longer crack lengths. Positive and negative  $K_{res}$  values were measured in  
 312 the X100 FSW, W1, and W3 coupons depending on crack position. The  $K_{res}$  values shown in Fig. 7a are a  
 313 weighted integral of residual stress (Fig. 6); therefore the slope of  $K_{res}$  versus  $a$  is positive when the  $\sigma_{res}$  is  
 314 positive and vice versa. **Figure 7b was created to show how the  $K_{res}$  values measured would superimpose**  
 315 **on the  $\Delta K_{app}$  values for an example of each material tested.**

316 Total stress ratio  $R_{tot}(a)$ , calculated using equation (3), is shown in Fig. 8a for all coupons. Note  
 317 that the  $R_{app}$  was equal to 0.5, therefore any deviation of  $R_{tot}(a)$  from 0.5 is direct influence of  $K_{res}$ , which  
 318 is quite substantial in some coupons. At longer crack lengths the  $R_{tot}(a)$  values approached 0.5 but at shorter

319 crack lengths a significant amount of variability was observed except for the X100 base metal which  
 320 exhibited  $R_{tot}(a) \sim R_{app} = 0.5$ . The X100A weld, X100A HAZ, and X100 FSW all exhibited  $R_{tot}(a)$  values  
 321 greater than 0.5 for the majority of the fatigue test. X100 W1, X100 W3, X100 W4 and X100 FSW HAZ  
 322 all exhibited  $R_{tot}(a)$  values less than 0.5. Of notable interest is the X100 W4 at short crack lengths which  
 323 actually exhibited negative R suggesting compression loading during portions of the fatigue test. This is  
 324 due to the extremely large negative  $K_{res}$  at short crack lengths. This also perhaps explains the unconventional  
 325 behavior of the  $da/dN$  vs  $\Delta K_{app}$  curve for the X100 W4 shown in Fig. 4 which exhibited very low fatigue  
 326 crack growth rates and discontinuities in the curve. Testing at negative R would have the effect of lowering  
 327 the FCGR substantially. Due to the presence of the notch and precrack in ESE(T) coupons, the majority of  
 328 the FCGR data were collected between 4 and 9 mm crack lengths. Therefore, because  $R_{tot}(a)$  is calculated  
 329 based on  $K_{max}$  and  $K_{min}$  data from FCGR curves, only the  $R_{tot}(a)$  values experienced in the tests are shown  
 330 (e.g. no  $R_{tot}(a)$  values were calculated from crack lengths less than 4 mm or longer than 9 mm except for  
 331 the X100 base metal which was performed on a C(T) coupon). **In Fig. 8b, the  $R_{tot}$  values was also plotted  
 332 as a function of  $\Delta K_{app}$ , similar to how  $K_{res}$  was plotted versus  $\Delta K_{app}$  in Fig. 7b in order to make easier visual  
 333 comparisons of the plots with Fig. 4.**



334  
 335 Figure 7 – Residual stress intensity factor ( $K_{res}$ ) as a function of crack length for X100 welds and base  
 336 metal. For each weld, two separate samples were measured, and the results are plotted, except for X100  
 337 W4. The periodicity observed in the gas metal arc welds is consistent with the individual passes present in  
 338 these multi-pass welds.



339

340 Figure 8 - Total stress ratio,  $R_{tot}(a)$ , as function of crack length for the X100 welds.  $R_{tot}$  values were  
 341 negative for X100 W4 for the majority of shorter crack lengths.

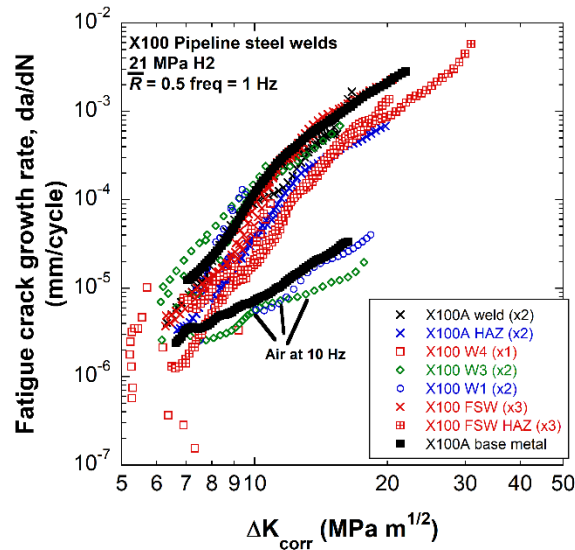
342

### 343 3.3 FCGR correction using $K_{res}$

344 Fatigue crack growth rate curves were corrected ( $da/dN$  vs.  $\Delta K_{corr}$ ) by removing the effects of  
 345 residual stress. This was accomplished by collapsing the data to a single  $K_{norm}$  curve according to equation  
 346 4 and then re-introducing the specified stress ratio  $\bar{R} = 0.5$  as described in section 2.5. The resulting FCGR  
 347 curves are shown in Fig. 9 for the X100 welds, HAZs, and base metal. The term  $\Delta K_{corr}$  is used to indicate  
 348 that the data have been corrected for residual stress. In addition, three curves in air for the X100A base  
 349 metal, X100 W1, and X100 W3 are shown for comparison. Similar to Fig. 4, duplicate (x2) or triplicate  
 350 (x3) test results are shown except for X100 W4 (x1) in which only a single test was performed.

351 In general, the FCGR curves exhibit greater overlap and occupy a tighter band when corrected for  
 352 residual stress as shown in Fig. 9 compared to the  $da/dN$  vs  $\Delta K_{app}$  data in Fig. 4. As would be expected, the  
 353 materials with the largest  $K_{res}$  exhibited the greatest shift in FCGR curves (e.g. X100 FSW HAZ and X100  
 354 W4). Because both had compressive residual stresses (e.g. negative  $K_{res}$ ), their  $R_{tot}(a)$  values were less than  
 355 0.5 and when plotted at the specified stress ratio  $\bar{R} = 0.5$ , the curves shifted to the left in  $\Delta K$ -space when  
 356 corrected. It is commonly observed that testing at higher  $R$  shifts the curve to the left and vice versa [26].  
 357 A comparison of the FCGRs in air also shows the data overlay better after corrected for residual stress (Fig.  
 358 9) than in the raw data (Fig. 4). The X100A base metal contained negligible residual stress and as a result  
 359 did not shift when corrected for residual stress; therefore, X100A base metal can serve as a reference curve  
 360 between the two figures (Fig. 4 and Fig. 9). It is interesting to note that the majority of FCGR curves in 21  
 361 MPa  $H_2$  fall below the X100A base metal data which suggests that in the absence of residual stress, the  
 362 welds and HAZs microstructures are not more susceptible to accelerated fatigue crack growth rate than the  
 363 base metal. However despite the reduction in variability in data, it is acknowledged that this correction  
 364 method for residual stress is not perfect and variability still exists as shown in Fig. 9. For example, a  
 365 common  $n$  value of 0.25 was used for all materials in Equations 4 and 5, despite only being calculated based  
 366 on X100 base metal data in air. Additionally, the large variations in residual stress results in large  
 367 fluctuations in  $R_{tot}$  values shown in Fig. 8a, and in the case of X100 W4, resulted in negative  $R$  values.

368 Therefore, the corrections imposed are meant to represent a best effort for removing residual stresses but  
369 are not without error.

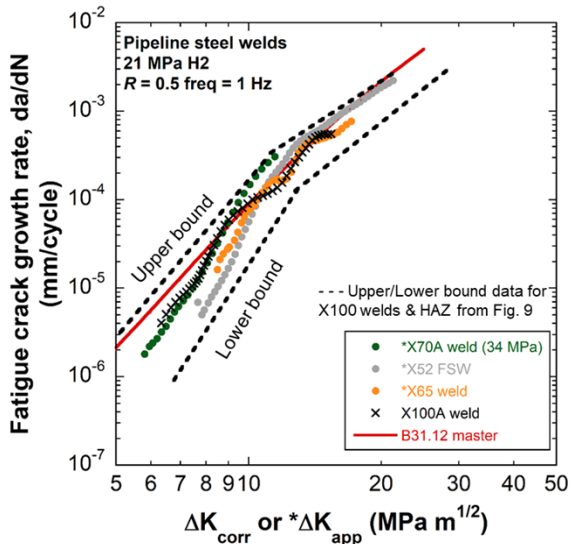


370  
371 Figure 9 – Fatigue crack growth rate curves ( $da/dN$  vs  $\Delta K_{corr}$ ) corrected for residual stress for X100 welds,  
372 base metal and HAZ tested in 21 MPa  $H_2$  at specified stress ratio  $\bar{R} = 0.5$  and 1 Hz.

373  
374 *3.4 Comparison of High Strength Welds with Low Strength Welds*

375 One motivation for investigating the fatigue behavior of higher strength welds in hydrogen was to  
376 determine their general susceptibility relative to lower strength grades more commonly used. In the  
377 literature [4, 12, 13], several lower strength pipeline welds have been tested in similar hydrogen  
378 environments; however, residual stress measurements have not been performed on the lower strength welds.  
379 Therefore, a true comparison of the residual stress-free FCGRs cannot be conducted. However, given that  
380 lower strength welds have a lower capacity for residual stress, it was thought that comparisons could be  
381 made between residual stress-free X100 weld FCGR curves and the non-corrected lower strength welds. **It**  
382 **should be noted that the FCGR data on lower strength welds found in refs [4, 12] were generated in the**  
383 **same laboratory as the current work and therefore should provide some consistency in procedures to allow**  
384 **for comparisons.** To simplify the comparison, Fig. 10 shows the upper and lower bound data for the X100  
385 welds and HAZ (extracted from Fig. 9) compared to lower strength welds from the literature [4, 12, 13]. In  
386 addition, the X100A weld was plotted in Fig. 10 along with the master design curve for pipeline steels  
387 found in the newly approved version of ASME B31.12 code. Currently, the B31.12 master curve can only  
388 be used for pipelines with **specified minimum yield stress** (SMYS) up to 482 MPa (70 ksi) operating up to  
389 21 MPa  $H_2$ . The lower strength welds [4, 12, 13] were tested at nominally the same conditions as the current  
390 study; however, residual stress measurements were not performed and therefore the plots are in the form of  
391  $da/dN$  vs  $\Delta K_{app}$ , indicated by the (\*). The X100A weld and the upper and lower bound curves are plotted  
392 with respect to  $\Delta K_{corr}$  which were corrected for residual stress. The lower strength welds exhibit very similar  
393 FCGRs and clearly fall within the upper and lower bounds as shown in Fig. 10. Furthermore, the ASME  
394 B31.12 design curve for pipelines falls close to the upper bound high strength weld data signifying that the  
395 B31.12 master curve may be sufficient to capture the majority of higher strength weld data. This suggests  
396 that higher strength welds without residual stress do not exhibit significantly greater susceptibility to

397 accelerated FCGR than lower grades containing residual stress. It also demonstrates that microstructural  
 398 differences do not appear to have a significant effect on the susceptibility to hydrogen-accelerated fatigue  
 399 crack growth and that the dominate effect in shifting FCGR curves is residual stress.



400  
 401 Figure 10 – Fatigue crack growth rate curves for lower strength welds compared to upper and lower bound  
 402 data of residual stress-free FCGR curves for high strength welds and HAZ (extracted from Fig. 9). Curves  
 403 for high strength welds (e.g. X100 welds) were corrected for residual stress and are therefore plotted versus  
 404  $\Delta K_{corr}$ . Lower strength welds are not corrected for residual stress and are plotted versus  $\Delta K_{app}$ . Welds of  
 405 X52 [4], X65 [12] and X70 [13] were all performed at  $R_{app} = 0.5$ . X100A weld and ASME B31.12 master  
 406 design curves are shown for comparison.

407  
 408 *3.5 Importance of Residual Stress Impacts on FCGR*

409 It was shown in the previous sections that residual stresses and  $K_{res}$  affect the total stress ratio,  
 410  $R_{tot}(a)$ , which shifts FCGR data found in coupon tests, e.g. higher  $R_{tot}$  shifts the FCGR higher and vice  
 411 versa. The literature [26, 27] also shows that  $K_{max}$  influences the onset of hydrogen accelerated fatigue crack  
 412 growth (HA-FCG) and  $K_{max}$  is also affected by  $K_{res}$ .

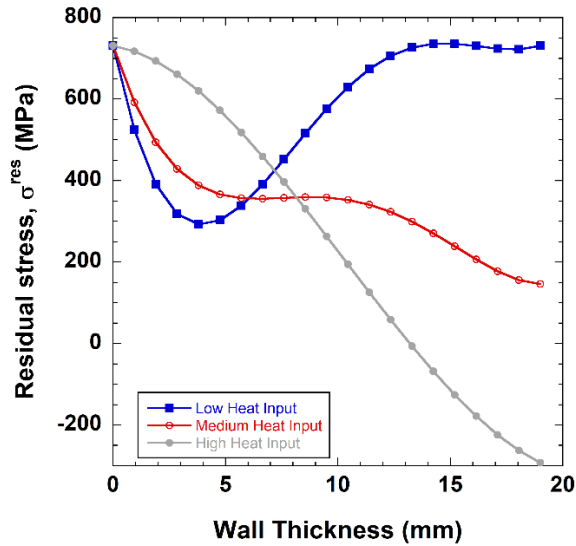
413 But, it is important to underscore that residual stress impacts fatigue engineering in two distinct  
 414 ways. First, residual stress effects occur in FCGR tests and it is useful to remove those effects so that FCGR  
 415 data are useful in design, for alloy-to-alloy comparisons, and to enable comparisons of intrinsic FCG  
 416 resistance in different regions of welded joints (e.g., base metal, weld, and HAZ). Second, welded  
 417 connections in structures have residual stresses that are distinct from those in coupons, and these residual  
 418 stress fields are often larger. Accounting for these two distinct contributions of residual stress is important,  
 419 and particularly for welds in higher strength materials because of their capacity to retain higher residual  
 420 stresses.

421 In the current study, residual stress and  $K_{res}$  were measured on rectangular ESE(T) coupons  
 422 extracted from approximately the mid-thickness of 19 mm thick pipe (Fig. 3). The levels of residual stress  
 423 are modest, with peak values of 20 to 40% of the base metal yield strength. The levels of  $K_{res}$  are also  
 424 modest, being less than 20 MPa  $m^{1/2}$ , because the residual stresses are small and because the stresses have

425 no net uniform or bending component (which must be the case in a free-standing coupon); in all cases the  
426 values of  $K_{res}$  decrease to negligible levels at long crack lengths. Residual stresses relax as a result of coupon  
427 removal, so the coupon residual stresses are most certainly different than those in the intact welded pipe.  
428 The difference between coupon and intact residual stress fields further reinforces the importance of  
429 removing the effect of residual stresses from the FCGR data as the residual stress effects are not  
430 representative of those in intact pipe welds.

431 Residual stresses in intact piping should be included in structural assessments and it is instructive  
432 to compare typical intact piping residual stress fields and corresponding  $K_{res}$  values to the data from the  
433 present coupons. Relevant welded piping assessment standards [28, 29] provide guidance on the magnitude  
434 and distribution of residual stress typical of piping weld joints. The guidance includes residual stress  
435 magnitude and spatial distribution depending on factors such as material strength, weld type, joint thickness,  
436 and heat input [28, 29]. Annex 9D.5 of API 579-1/ASME FFS-1 [29] provides equations for estimated  
437 residual stress perpendicular to the weld, based on strength and heat input. Heat input ( $\dot{q}$ ) normalized by  
438 pipe thickness is categorized as high ( $> 120 \text{ J/mm}^2$ ), medium ( $> 50 \text{ J/mm}^2$ ), or low ( $< 50 \text{ J/mm}^2$ ). All of  
439 welds in this study, which we have data for, have low heat input ranging from 33 to 46  $\text{J/mm}^2$ . Fig. 11  
440 shows these residual stress distributions, assuming  $\sigma_{YS} = 731 \text{ MPa}$  for X100 base metal and a pipe thickness  
441 of 19 mm. When compared to the residual stresses measured in the removed ESE(T) coupons (Fig. 6), all  
442 of the **simulated residual stresses for intact pipes** in Fig. 11 have large magnitude. They also include  
443 significant uniform (low and medium heat input) and bending (high heat input) fields that are absent in the  
444 coupon residual stresses (they must be absent in a free-standing coupon, on account of equilibrium  
445 constraints). Figure 11 also shows that the low heat input weld has the most conservative recommended  
446 residual stress distribution (e.g. largest average tensile residual stresses throughout the thickness).

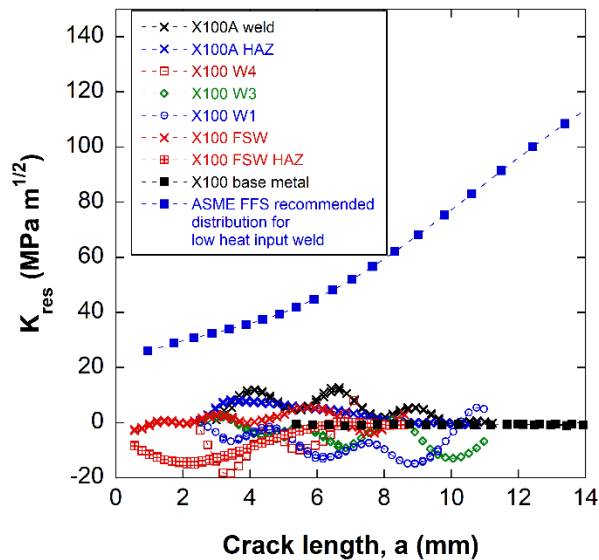
447 Given the large differences in residual stress, values of  $K_{res}$  in a cracked pipe would also differ  
448 greatly from the values of  $K_{res}$  found in the FCGR coupons. Using the low heat input residual stress field  
449 in Fig. 11 we computed  $K_{res}$  using the weight function method from ASME Section XI Appendix A [30]  
450 assuming a circumferential flaw driven by the axial residual stress. The flaw shape was assumed semi-  
451 elliptical with an aspect ratio of 1/3 (depth divided by total surface length), which is conservative according  
452 to ASME BPVC Section VIII Div 3 Article KD-4 [31]. Fig. 12 compares  $K_{res}$  for the pipe weld to  $K_{res}$   
453 measured in the removed FCGR coupons. This shows clearly that  $K_{res}$  in the FCGR coupons differs  
454 substantially from what should be expected in a pipe weld, being far lower in the coupons, and suggest the  
455 significant release of residual stress occurring upon coupon extraction.



456

457 Figure 11 – Recommended residual stress ( $\sigma^{\text{res}}$ ) distributions perpendicular to the weld for low, medium,  
 458 and high heat input welds as a function of position through-wall. Plot was developed using  $YS=731$  MPa,  
 459 and  $t = 19$  mm.

460



461

462 Figure 12 –  $K_{\text{res}}$  vs crack length for X100 welds, HAZ, and base metal compared to  $K_{\text{res}}$  recommended  
 463 distribution for full thickness low heat input weld according to API 579/ASME FFS-1 [29].  $K_{\text{res}}$  are in the  
 464 direction radial direction of the pipe, except for the X100 base metal which is in the circumferential  
 465 direction.  $K_{\text{res}}$  plotted for X100 welds, HAZ, and BM are identical to those in Fig. 7.

466

#### 467 4. Conclusions

468 Five different high strength welds were fabricated from X100 base metal for the purpose of  
 469 measuring fatigue crack growth rates (FCGR) in high pressure hydrogen gas. Test coupons were extracted

470 from the weld regions along with select heat affected zones and fatigue crack growth rates were measured  
471 in 21 MPa H<sub>2</sub> at R<sub>app</sub> =0.5 and frequency of 1 Hz. Identical test coupons were used to measure residual  
472 stresses by means of the slitting method. Residual stress, K<sub>res</sub>, measurements were used to calculate the  
473 effect on stress ratio, R<sub>tot</sub>(a), and the FCGR curves were corrected to allow for residual stress-free FCGR  
474 curves. The residual stress-free curves displayed less variability than the raw data containing residual stress.  
475 Lower strength weld FCGR data from the literature were comparable to the high strength X100 welds which  
476 demonstrated, **that despite differences in strength and microstructure**, high strength welds are no more  
477 susceptible to hydrogen accelerated fatigue crack growth than the lower strength welds. An analysis was  
478 performed to compare the residual stress values measured via the slitting method on the test coupons versus  
479 recommended residual stress distributions from ASME FFS [29] for low heat input welds. The results  
480 showed that the residual stresses measured in the test coupons were significantly lower than the recommend  
481 residual stress distributions for an **intact welded pipe**, highlighting that significant stress relaxation can  
482 occur through test coupon extraction. Quantifying and removing the residual stresses in FCGR data offers  
483 the greatest utility by providing a neutral starting ground for comparisons and design guidance when  
484 residual stress effects are to be considered.

485

## 486 5. Acknowledgments

487 The authors would like to thank the following people and funding agencies for their contributions to this  
488 work over the years. We would like to thank the technical support of the Hydrogen Effects on Materials  
489 Laboratory (HEML) at Sandia in Livermore, CA, specifically, Jeff Campbell, Brendan Davis, John Benton.  
490 We acknowledge the technical support from Doug Kyle and Zhenggang Wu of ORNL for fabrication and  
491 characterization of the welds. Special thanks to Minh N. Tran (University of California, Davis) for  
492 computing residual stress intensity factors for the pipeline flaws. In addition, we would like to thank some  
493 collaborators from other institutions: Andy Slifka (NIST), Elizabeth Drexler (NIST, retired), Robert Amaro  
494 (Southern Company). This work was funded by the Fuel Cell Technology Office of DOE. Sandia National  
495 Laboratories is a multi-mission laboratory managed and operated by National Technology & Engineering  
496 Solutions of Sandia, LLC, a wholly owned subsidiary of Honeywell International Inc., for the U.S.  
497 Department of Energy's National Nuclear Security Administration under contract DE-NA0003525.

498

499

## 500 References:

501

- 502 [1] *Hydrogen Standardization Interim Report for Tanks, Piping, and Pipelines*, ASME, 2005.  
503 [2] "U.S. DRIVE Hydrogen Delivery Technical Team Roadmap."  
504 [https://www.energy.gov/sites/prod/files/2017/08/f36/hdtt\\_roadmap\\_July2017.pdf](https://www.energy.gov/sites/prod/files/2017/08/f36/hdtt_roadmap_July2017.pdf) (accessed.  
505 [3] J. A. Ronevich, C. R. D'Elia, and M. R. Hill, "Fatigue crack growth rates of X100 steel welds in high  
506 pressure hydrogen gas considering residual stress effects," *Engineering Fracture Mechanics*, vol.  
507 194, pp. 42-51, 2018/05/01/ 2018, doi: <https://doi.org/10.1016/j.engfracmech.2018.02.030>.  
508 [4] J. A. Ronevich, B. P. Somerday, and Z. Feng, "Hydrogen accelerated fatigue crack growth of  
509 friction stir welded X52 steel pipe," *International Journal of Hydrogen Energy*, vol. 42, no. 7, pp.  
510 4259-4268, 2017/02/16/ 2017, doi: <https://doi.org/10.1016/j.ijhydene.2016.10.153>.  
511 [5] J. A. Ronevich, B. P. Somerday, and C. San Marchi, "Effects of microstructure banding on  
512 hydrogen assisted fatigue crack growth in X65 pipeline steels," *International Journal of Fatigue*,  
513 vol. 82, no. Part 3, pp. 497-504, 2016/01/01/ 2016, doi:  
514 <https://doi.org/10.1016/j.ijfatigue.2015.09.004>.

- 515 [6] R. L. Amaro, N. Rustagi, K. O. Findley, E. S. Drexler, and A. J. Slifka, "Modeling the fatigue crack  
516 growth of X100 pipeline steel in gaseous hydrogen," *International Journal of Fatigue*, vol. 59, no.  
517 0, pp. 262-271, 2014, doi: <http://dx.doi.org/10.1016/j.ijfatigue.2013.08.010>.
- 518 [7] A. J. Slifka *et al.*, "Fatigue crack growth of two pipeline steels in a pressurized hydrogen  
519 environment," *Corrosion Science*, vol. 78, no. 0, pp. 313-321, 2014, doi:  
520 <http://dx.doi.org/10.1016/j.corsci.2013.10.014>.
- 521 [8] R. L. Amaro, E. S. Drexler, and A. J. Slifka, "Fatigue crack growth modeling of pipeline steels in  
522 high pressure gaseous hydrogen," *International Journal of Fatigue*, vol. 62, no. 0, pp. 249-257,  
523 2014, doi: <http://dx.doi.org/10.1016/j.ijfatigue.2013.10.013>.
- 524 [9] A. J. Slifka *et al.*, "Fatigue Measurement of Pipeline Steels for the Application of Transporting  
525 Gaseous Hydrogen," *Journal of Pressure Vessel Technology*, vol. 140, no. 1, pp. 011407-011407-  
526 12, 2017, doi: 10.1115/1.4038594.
- 527 [10] "Pipeline Accident Report NTSB/PAR-11/01 Pacific Gas and Electric Company Natural gas  
528 Transmission Pipeline Rupture and Fire, San Bruno, California," 2011.
- 529 [11] J. Ronevich and B. Somerday, "Hydrogen-Accelerated Fatigue Crack Growth in Arc Welded X100  
530 Pipeline Steel," in *Materials Performance in Hydrogen Environments: Proceedings of the 2016*  
531 *International Hydrogen Conference*, Jackson Hole, WY, B. P. Somerday and P. Sofronis, Eds.,  
532 2016: ASME, pp. 219-227.
- 533 [12] J. A. Ronevich and B. P. Somerday, "Assessing Gaseous Hydrogen Assisted Fatigue Crack Growth  
534 Susceptibility of Pipeline Steel Weld Fusion Zones and Heat Affected Zones," *Materials*  
535 *Performance and Characterization*, vol. 5, no. 3, pp. 290-304, 2016, doi: 10.1520/MPC20150057.
- 536 [13] A. Slifka *et al.*, "Measurements of Fatigue Crack Growth Rates of the Heat-Affected Zones of  
537 Welds of Pipeline Steels," presented at the Proceedings of ASME 2015 Pressure Vessels and  
538 Piping Conference, Boston, MA, 2015.
- 539 [14] Z. Feng, S. A. David, D. A. Tzelepis, and X. Yu, "Welding Method for Hydrogen Embrittlement  
540 Control," USA, 2016.
- 541 [15] *E647-11 Standard Test Method for Measurement of Fatigue Crack Growth Rates*, ASTM, West  
542 Conshohocken, PA, 2011.
- 543 [16] B. P. Somerday, J. A. Campbell, K. L. Lee, J. A. Ronevich, and C. San Marchi, "Enhancing safety of  
544 hydrogen containment components through materials testing under in-service conditions,"  
545 *International Journal of Hydrogen Energy*, vol. 42, pp. 7314-7321, 2017, doi:  
546 10.1016/j.ijhydene.2016.04.189.
- 547 [17] *B31.12 Hydrogen Piping and Pipelines*, ASME, New York, NY, 2011.
- 548 [18] B. P. Somerday, P. Sofronis, K. A. Nibur, C. San Marchi, and R. Kirchheim, "Elucidating the  
549 variables affecting accelerated fatigue crack growth of steels in hydrogen gas with low oxygen  
550 concentrations," *Acta Materialia*, vol. 61, no. 16, pp. 6153-6170, 2013, doi:  
551 <http://dx.doi.org/10.1016/j.actamat.2013.07.001>.
- 552 [19] M. B. Prime, "Residual stress measurement by successive extension of a slot: The crack  
553 compliance method," *Applied Mechanics Reviews*, vol. 52, no. 2, pp. 75-96, 1999.
- 554 [20] M. R. Hill, "The Slitting Method," in *Practical Residual Stress Measurement Methods*, G. S.  
555 Schajer Ed. West Sussex, UK: John Wiley & Sons, 2013, ch. 4, pp. 89-108.
- 556 [21] G. S. Schajer and M. B. Prime, "Use of Inverse Solutions for Residual Stress Measurements,"  
557 *Journal of Engineering Materials and Technology*, vol. 128, no. 3, pp. 375-382, 2006, doi:  
558 10.1115/1.2204952.
- 559 [22] H. J. Schindler, W. Cheng, and I. Finnie, "Experimental determination of stress intensity factors  
560 due to residual stresses," *Experimental Mechanics*, journal article vol. 37, no. 3, pp. 272-277,  
561 September 01 1997, doi: 10.1007/bf02317418.

- 562 [23] H. J. Schindler and P. Bertschinger, "Some steps towards automation of the crack compliance  
563 method to measure residual stress distributions," in *Fifth International Conference on Residual*  
564 *Stress*, 1997, pp. 682-687.
- 565 [24] J. K. Donald and D. A. Lados, "An integrated methodology for separating closure and residual  
566 stress effects from fatigue crack growth rate data," *Fatigue & Fracture of Engineering Materials*  
567 *& Structures*, vol. 30, no. 3, pp. 223-230, 2007, doi: doi:10.1111/j.1460-2695.2006.01081.x.
- 568 [25] M. James, K. Maciejewski, G. Wang, D. Ball, and R. Bucci, "A Methodology for Partitioning  
569 Residual Stress Effects From Fatigue Crack Growth Rate Test Data," 2016.
- 570 [26] J. K. Donald, G. H. Bray, and R. W. Bush, *Introducing the Kmax sensitivity concept for correlating*  
571 *fatigue crack growth data*. The Minerals, Metals and Materials Society, Warrendale, PA, 1997,  
572 pp. 123-141.
- 573 [27] S. Suresh and R. O. Ritchie, "Mechanistic dissimilarities between environmentally influenced  
574 fatigue-crack propagation at near-threshold and higher growth rates in lower strength steels,"  
575 *Metal Science*, vol. 16, pp. 529-538, 1982.
- 576 [28] *BS7910, Guide to methods for Assessing the Acceptability of Flaws in Metallic Structures*, B. S.  
577 Institution, 2015.
- 578 [29] *API 579-1/ASME FFS-1 2016 Fitness-For-Service*, ASME/API, 2016.
- 579 [30] *ASME BPVC Section XI Appendix A*, ASME, 2017.
- 580 [31] *ASME BPVC Section VIII Div 3 Article KD-4*, ASME, 2013.